

Multi-Modal Masked Pre-Training for Monocular Panoramic Depth Completion

Zhiqiang Yan¹, Kun Wang¹, Xiang Li¹, Zhenyu Zhang²,
Jun Li^{1✉}, and Jian Yang^{1✉}

¹PCA Lab*, Nanjing University of Science and Technology, China
{Yanzq,kunwang,xiang.li,implus,junli,csjyang}@njjust.edu.cn

²Tencent YouTu Lab zhangjesse@foxmail.com

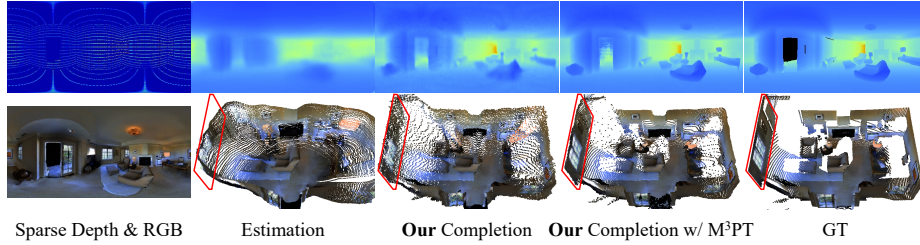


Fig. 1. Comparisons of the predicted depth and 3D reconstruction results between panoramic depth estimation (with RGB) and completion (with RGB and sparse depth).

Abstract. In this paper, we formulate a potentially valuable panoramic depth completion (PDC) task as panoramic 3D cameras often produce 360° depth with missing data in complex scenes. Its goal is to recover dense panoramic depths from raw sparse ones and panoramic RGB images. To deal with the PDC task, we train a deep network that takes both depth and image as inputs for the dense panoramic depth recovery. However, it needs to face a challenging optimization problem of the network parameters due to its non-convex objective function. To address this problem, we propose a simple yet effective approach termed M³PT: multi-modal masked pre-training. Specifically, during pre-training, we simultaneously cover up patches of the panoramic RGB image and sparse depth by shared random mask, then reconstruct the sparse depth in the masked regions. To our best knowledge, it is the first time that we show the effectiveness of masked pre-training in a multi-modal vision task, instead of the single-modal task resolved by masked autoencoders (MAE). Different from MAE where fine-tuning completely discards the decoder part of pre-training, there is no architectural difference between the pre-training and fine-tuning stages in our M³PT as they only differ in the prediction density, which potentially makes the transfer learning more convenient and effective. Extensive experiments verify the effectiveness

* PCA Lab, Key Lab of Intelligent Perception and Systems for High-Dimensional Information of Ministry of Education, and Jiangsu Key Lab of Image and Video Understanding for Social Security, Nanjing University of Science and Technology.

of M³PT on three panoramic datasets. Notably, we improve the state-of-the-art baselines by averagely 26.2% in RMSE, 51.7% in MRE, 49.7% in MAE, and 37.5% in RMSElog on three benchmark datasets.

Keywords: 360° depth completion, multi-modal masked pre-training, network optimization, shared random mask, 3D reconstruction

1 Introduction

Panoramic depth perception (see Table 1) has received increasing attention in both academic and industrial communities due to its crucial role in a wide variety of downstream applications, such as virtual reality [2], scene understanding [63], and autonomous navigation [22]. With the development of hardware devices, panoramic 3D cameras become easier and cheaper to capture both RGB and depth (RGB-D) data with 360° field of view (FoV). Depending on the captured RGB images, all recent perception technologies [51,63,30,41,82,92,4], to the best of our knowledge, concentrate on panoramic depth estimation (PDE) that predicts dense depth from a single 360° RGB image. In this paper, we focus on exploring the 360° RGB-D pairs for the panorama perception with an effective pre-training strategy. We show our motivations as follows:

Two Motivations for Panoramic Depth Completion (PDC). *One is the 360° depth maps with missing areas.* During the collection process, the popular panoramic 3D cameras (e.g., Matterport Pro2¹ and FARO Focus²) still produce 360° depth with missing areas when facing bright, glossy, thin or far surfaces, especially indoor rooms in Figure 2. These depth maps will result in a poor panorama perception. To overcome this problem, we consider a new panoramic depth completion task, completing the depth channel of a single 360° RGB-D pair captured from a panoramic 3D camera. *Another is an experimental investigation that in contrast with PDE, PDC is much fitter for the panoramic depth perception.* For simplicity and fairness, we directly employ the same network architectures (e.g., UniFuse [30]) to estimate or complete the depth map. Figure 7 reports that the PDC has much lower root mean square error than PDE. Furthermore, Figure 1 shows that the PDC can recover more precise 360° depth values, leading to better 3D reconstruction. This observation reveals that PDC is more important than PDE for 3D scene understanding.

One Motivation for Pre-Training. When using deep networks to perceive the depth information, there is a challenging problem: *how to optimize the parameters of the deep networks?* It is well-known that the objective function is highly non-convex, resulting in many distinct local minima in the network parameter space. Although the completion can lead to better network parameters and higher accuracy on the depth perception, it is still not to satisfy practical needs of the 3D reconstruction. Here, we are inspired by the greedy layer-wise pre-training technology [18,40] that stacks two-layer unsupervised autoencoders

¹ <https://matterport.com/cameras/pro2-3d-camera>

² <https://www.faro.com/en/Products/Hardware/Focus-Laser-Scanners>

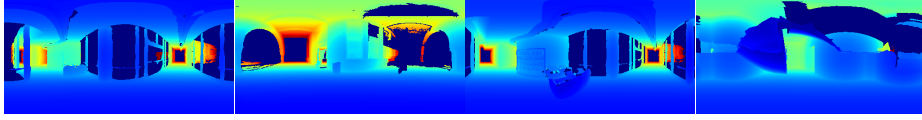


Fig. 2. Panoramic depth maps with large missing areas shown in darkest blue color.

to initialize the networks to a point in parameter space, and then fine-tunes them in a supervised setting. This technology drives the optimization process more effective, achieving a ‘good’ local minimum. Recently, the single-modal masked autoencoders [25,76] are also applied into object detection and semantic segmentation, achieving amazing improvements on their benchmarks. These interpretations and improvements motivate us to explore a new pre-training technology for the multi-modal panoramic depth completion.

In this paper, we propose a Multi-Modal Masked Pre-Training (M³PT) technology to directly initialize all parameters of deep completion networks. Specifically, the key idea of M³PT is to employ a shared random mask to simultaneously corrupt the RGB image and sparse depth, and then use the invisible pixels of the sparse depth as supervised signal to reconstruct the original sparse depth. After this pre-training, no-masked RGB-D pairs are fed into the pre-trained network supervised by dense ground-truth depths. Different from the layer-wise pre-training [18], M³PT is to pre-train all layers of the deep network. Compared to MAE [25], M³PT has no architectural difference between the pre-training and fine-tuning stages, where they differ in only the prediction density of target depth. This characteristic probably makes it convenient and effective for the transfer learning, including but not limited to the multi-modal depth completion, denoising, and super-resolution guided by RGB images. In summary, our contributions are as follows:

- We introduce a new panoramic depth completion (PDC) task that aims to complete the depth channel of a single 360° RGB-D pair captured from a panoramic 3D camera. To the best of our knowledge, we are the first to study the PDC task to facilitate 360° depth perception.
- We propose the multi-modal masked pre-training (M³PT) for the multi-modal vision task. Different from the layer-wise pre-training [18] and MAE [25], M³PT is to pre-train all layers of the deep network, and does not change the network architecture in the pre-training and fine-tuning stages.
- On three benchmarks, *i.e.*, Matterport3D [2], Stanford2D3D [3], and 3D60 [93], extensive experiments demonstrate that (i) PDC achieves higher accuracy of panoramic depth perception than PDE, and (ii) our M³PT technology achieves the state-of-the-art performance.

2 Related Work

Since this paper aims to learn the new task of monocular panoramic depth completion, we report three related but different topics whose detailed differences are

Task	Depth Estimation	Depth Completion	Panoramic Depth Estimation	Panoramic Depth Completion
New task	No	No	No	Yes
Data FoV	<180°	<180°	360°	360°
Data modal	RGB	RGB-D	RGB	RGB-D
Camera	perspective	perspective	panoramic	panoramic
Target	depth	depth	depth & 3D reconstruction	depth & 3D reconstruction

Table 1. Comparisons of different depth related tasks. FoV denotes the field of vision.

listed in Table 1. First, we review depth estimation methods based on color images with limited FoV. Second, we introduce depth completion approaches that input single RGB-D pairs with narrow FoV. At last, we elaborate on panoramic depth estimation works which predict 360° depths from panoramic color images.

2.1 Monocular Depth Estimation with Limited FoV

Previous monocular depth estimation methods, including supervised and unsupervised counterparts, mainly pay attention to predicting dense depths for sparse ones a limited FoV that is less than 180°. The research concerned with depth estimation can trace back to [57]. After that, lots of supervised works [16,56,83,84,89,36] have been proposed, which largely develop the domain. For example, Lee *et al.* [35] improve the performances of other works by designing the local planer guidance layer located at multiple stages in decoding phase. Aich *et al.* [1] attempt to address the limitation of effectively integrating local and global information by bidirectional attention design. Qiao *et al.* [52] jointly perform depth estimation and segmentation to tackle the long-standing and challenging inverse projection problem in vision. Zhang *et al.* [85] jointly study depth, surface normal, and semantic segmentation via pattern-affinitive propagation. To deal with poor driving conditions, Wang *et al.* [71] argue that weak textures and inconsistent illumination in night environment result to bad depth estimation and design three strategies to tackle the issue. Liu *et al.* [44] tackle the depth estimation in challenging night condition by domain separation.

Further, to reduce manual labeling costs, Zhou *et al.* [90] present the first unsupervised depth estimation framework, where the view synthesis is introduced as the supervisory signal during training. This excellent work tends to spark a new wave of research. Since then, plenty of unsupervised approaches [21,6,59,87,32,24] have thrived over the past five years, all of which abandon the expensive depth annotations. For example, for one thing, to break down the assumption in [90] that scene is static while moving objects violate it, optical flow [95,54] and segmentation models [7,22,49] are carried out to compensate and mask pixels nearby moving objects respectively. For another thing, to handle the issue of occlusion, MonoDepth2 [21] presents the minimum reprojection loss. In addition, geometry priors such as surface normals [81] and semantic clues [49] are introduced to robust unsupervised depth estimation models. Different from these approaches based on FoV-limited color images, we focus on 360° RGB-D to reconstruct panoramic depth and 3D reconstruction.

2.2 Monocular Depth Completion with Limited FoV

Existing monocular depth completion methods primarily focus on sparse depths and color images with a narrow FoV less than 180°. Up to now, based on the commonly used KITTI [67] and NYUv2 [60] datasets, a great deal of methods have been proposed to tackle the task, which can be broadly divided into depth-only [67,13,48,17] and multi-sensor fusion based [12,11,58,79,23,80,42] categories. For example, the literatures [29,68] take sparse depths as the only input to recover dense ones without using color images. Further, Lu *et al.* [47] use color images as auxiliary supervision during training and is discarded when testing. Recently, as technology quickly develops, multi-modal information can be captured by sensors, which is beneficial for depth completion. For example, S2D [48] directly concatenate RGB-D pairs and feed them into networks, contributing to promising improvement. Li *et al.* [39] propose multi-scale guided cascade hourglass network to handle diverse patterns. PENet [27] proposes to refine depth recovery at three stages. FCFRNet [43] designs channel-shuffle technology to enhance RGB-D feature fusion. GuideNet [64] proposes dynamic convolution to adaptively generate convolution kernels according to color image contents. ACMNet [86] conducts graph propagation to extract multi-modal representations. Furthermore, DeepLiDAR [53] and PwP [77] jointly utilize color images, surface normals, and sparse depths to recover dense depth. FusionNet [68] and Zhu *et al.* [91] present to estimate uncertainty for robust recovery. NLSPN [50] and DSPN [78] introduce recurrent non-local and dynamic spatial propagation networks, which significantly improve depth accuracy nearby object boundaries.

In addition, several unsupervised depth completion works [74,33,73,72,66] also contribute to the development of this domain. For example, KBNet [75] proposes the fantastic calibrated backprojection network which achieves very superior performances. However, as mentioned above these methods are designed for dense depth recovery from FoV-limited sparse depth, whilst we aim to learn 360° depth completion and 3D reconstruction from panoramic RGB-D input.

2.3 Monocular Depth Estimation with Full FoV

Given panoramic color images, current monocular panoramic depth estimation works mainly devote into predicting 360° depths and 3D reconstructions. This topic springs up as soon as the large indoor panoramic datasets Matterport3D [8] and Stanford2D3D [3] are constructed in 2017. For this domain in the last five years, supervised methods play a primary role while unsupervised approaches develop slowly. Next we will introduce each of them.

Supervised category: In 2018, OmniDepth [94] synthesizes 360° data with high-quality ground-truth depth annotations by rendering existing datasets. DistConv [65] proposes distortion-aware convolutional filters to address the inherent distortion of equirectangular projection (EPR) panoramic data. In 2019, Eder *et al.* [15] utilize surface normal and plane boundaries to train a plane-aware network to benefit depth estimation. SpherePHD [37,38] explores a new data representation via spherical polyhedron, which resolves the shape distortion

of spherical panoramas. In 2020, Jin *et al.* [31] and Feng *et al.* [19] use geometric priors to help with depth estimation. Wang *et al.* [70] adopt a two-branch network leveraging EPR and cubemap projections, which are the two most common data forms. In 2021, PanoDepth [41] develops a two-stage framework containing view synthesis and stereo matching. UniFuse [30] further improves [70] with better accuracy and fewer parameters. SliceNet [51] transforms the EPR data into slice-based representation, which can tackle the inherent distortion. Sun *et al.* [63,62] focus on horizontal and vertical contents of a scene for 3D reconstruction. 360MonoDepth [55] projects the high-resolution spherical image into tangent image for efficient training. In 2022, SegFuse [20] utilizes geometric and temporal consistency to constraint depth recovery. GLPanoDepth [4] employs vision transformer and CNNs to encode cubemap and spherical images respectively, obtaining global-to-local representation of panoramas. ACDNet [92] designs adaptively combined dilated convolution to extend receptive field in the EPR and achieves state-of-the-art performances.

Unsupervised category: In 2019, Nikolaos *et al.* [93] explore spherical view synthesis for monocular 360° depth estimation in a self-supervised manner. In 2021, OlaNet [34] adopts the distortion-aware view synthesis, atrous spatial pyramid pooling, and L1-norm regularized smooth term to effectively and robustly deal with self-supervised panoramic depth estimation. Zhou *et al.* [88] combine supervised and unsupervised learning methods to facilitate network training. In 2022, Yun *et al.* [82] propose a self-supervised method based on gravity-aligned videos. Similarly, they also utilize the complementarity of supervised and self-supervised learning to improve their models’ robustness.

Different from them that only utilize 360° color image, our goal is to recover dense depth and 3D reconstruction from the aligned 360° color image and sparse depth, which could help improve the accuracy with large margins.

2.4 Masked Image Encoding for Vision Tasks

Recently, several Transformer [69] based approaches [10,14,5,76,25] have proved it effective to learn representations from masked images. Specifically, iGPT [10] trains a sequence Transformer to auto-regressively predict unknown pixels. ViT [14] conducts masked patch prediction to learn mean color. BEiT [5] presents to predict tokenization. SimMIM [76] and MAE [25] propose to recover raw pixels of randomly masked patches by a lightweight one-layer head and an asymmetric decoder, respectively. In contrast to them, our M³PT is technically designed for multi-modal vision tasks instead of the single-modal image-based recognition.

3 Method

In this section, we first introduce how to synthesize sparse depth data and then elaborate on the multi-modal masked pre-training strategy.

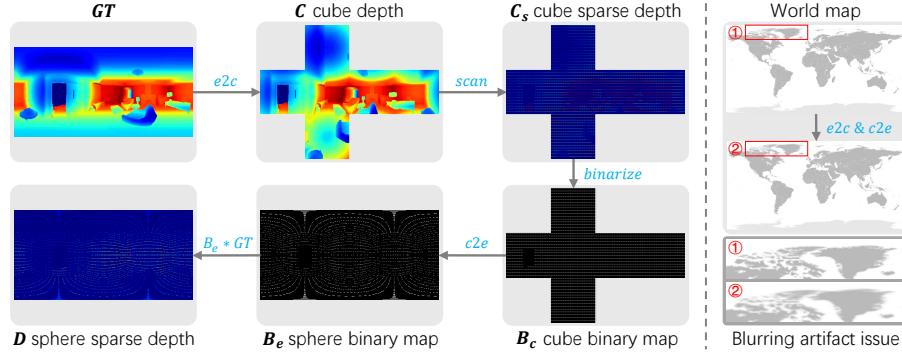


Fig. 3. A flowchart of data synthesis (left) and an example of the blurring artifact issue (right) that has negative effects on data processing. Best color of view.

3.1 Data Synthesis

All existing panoramic datasets do not provide sparse depth for 360° depth completion task. However, the sparse depth data can be possibly captured by some actual products such as Matterport Pro2 and FARO Focus 3D cameras. Limited by the lack of these hardware devices, in this paper, we imitate the principle of laser scanning to produce 360° sparse depth sampled from the dense ground-truth depth annotation, aiming at synthesizing the sparse depth data that matches the actual products as much as possible. The sampling principle is similar to that of KITTI benchmark [67] which provides depth with about 7% density captured by 64-line LiDAR scanning.

As illustrated in the left of Figure 3, the ground-truth depth GT is stored in spherical view by equirectangular projection, which brings inherent distortion. Hence, it's inaccurate to produce sparse depth directly based on GT in scanning mode. As an alternative, we first project the equirectangular GT into cubical map C by $e2c$ function, ignoring the inherent distortion. Next, we generate cube sparse depth C_s via imitating the laser scanning, *e.g.*, taking one pixel for every eight pixels horizontally and one pixel for every two pixels vertically. Then C_s is binarized to obtain cube binary map B_c . B_c is thus converted into B_e by $c2e$ function. Finally, we acquire the desired sparse depth D multiply B_e by GT . The process can be simply defined as:

$$D = B_e * GT, \quad (1)$$

where $B_e = f(B_c | C_s, C, GT)$, $f(\cdot)$ refers to the combination of $e2c$, $scan$, $binarize$, and $c2e$. The details of $e2c$ and $c2e$ functions refer to this project³.

Note that, it is theoretically possible to use $c2e$ to directly project the cubical C_s into the equirectangular D . However, this would lead to blurring artifacts in the polar region, as evidenced in the right part of Figure 3. Instead, we choose to project a binary map and then use it to accurately sample valid points from GT . In this way, our method can reduce error pixels as much as possible.

³ <https://github.com/sunset1995/py360convert>

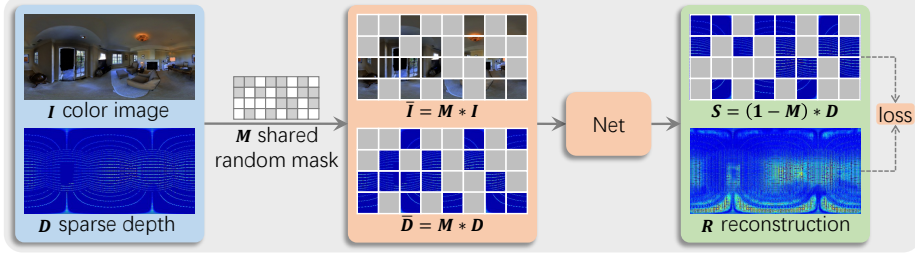


Fig. 4. Our M³PT pipeline. During pre-training, the input color image I and sparse depth D are masked out by the shared random mask M , obtaining \bar{I} and \bar{D} respectively. Then \bar{I} and \bar{D} are fed into a network to predict the depth reconstruction R , supervised by the signal S which is the complementary set of \bar{D} in D . After pre-training, with I and D as input, the network with learned initial weights is applied to recover target depths supervised by dense ground-truth depth annotations.

3.2 Multi-Modal Masked Pre-Training

As shown in Figure 4, our multi-modal masked pre-training (M³PT) for 360° depth completion is a simple strategy that reconstructs the sparse depth signal given partial observations of the RGB-D pair under shared random mask. Here we introduce the key components of M³PT and explicitly analyze the differences between recent visual masked pre-training approaches (*e.g.*, MAE [25], SimMIM [76]) and M³PT.

Shared random mask. Different from MAE where masking is performed on single RGB data, we propose to mask both RGB image and sparse depth with the *shared random mask* to produce incomplete RGB-D pair as input for pre-training. In fact, there are other options of masking strategies for PDC task, including (i) only mask the RGB image, (ii) only mask the sparse depth, and (iii) mask both RGB image and sparse depth but with different random masks. Unfortunately, all of these strategies have a risk of leaking information from another modality, preventing the pre-training task from learning robust semantics based on the multi-modal context. We will show the comparisons between different masking strategies later in the experimental part.

Backbone. Our method is flexible and can be applied to any existing approach which receives the RGB-D pair as input. In this paper, we mainly choose GuideNet [64] as backbone for the majority of our experiments. In addition, we also test the effectiveness of M³PT using UniFuse [30] and HoHoNet [63]. Note that there is no need to design extra modules (*e.g.*, a decoder) for the architectures of these existing approaches, even when they have an additional pre-training stage in M³PT. It is because that the regression targets are physically similar between pre-training and fine-tuning stages. See more details in the ‘Reconstruction target’ part as follows.

Reconstruction target. The reconstruction target of M³PT is the sparse depth on the masked regions. It is quite different from the popular masked pre-training methods [25, 76] in vision where the missing image pixels are predicted. Compared to the vision pre-training counterparts [25, 76], this design has two

obvious advantages: (i) it closes the gap between pre-training and fine-tuning tasks, as they differ only in the prediction density; (ii) it leads to *no architectural modification* between pre-training and fine-tuning stages, which can potentially make the transfer learning more smooth and effective.

4 Experiments

In this section, we first report related datasets and metrics. Then, extensive ablation studies are conducted to verify the effectiveness of the proposed method. Finally, we compare our approach against other state-of-the-art (SoTA) works on three datasets. **Note that all the methods involved here are retrained FROM SCRATCH with publicly available codes.**

4.1 Datasets

We conduct our experiments on three commonly used benchmark datasets of real world, *i.e.*, Matterport3D⁴ [2], Stanford2D3D⁵ [3], and 3D60⁶ [93]. Matterport3D is a scanned dataset collected by Matterport’s Pro 3D camera. The latest Matterport3D (512×256) consists of 7,907 panoramic RGB-D pairs, of which 5636 for training, 744 for validating, and 1527 for testing. Stanford2D3D is composed of 1,413 panoramic color images and corresponding depth maps, whose training and testing splits contain 1,040 and 373 RGB-D pairs, respectively. We resize them to 512×256 . 3D60 is initially made up of Matterport3D, Stanford2D3D, and SunCG [61]. But now it skips the entire SunCG dataset considering legal matters. As a result, the latest 3D60 (512×256) consists of 6,669 RGB-D pairs for training, 906 for validating, and 1831 for testing, 9,406 in total.

4.2 Metrics

Following previous works [63,51,82,92], we use five common and standard metrics to evaluate our methods, including MRE, MAE, RMSE, RMSElog, and δ_i ($i = 1.25, 1.25^2, 1.25^3$). Please refer to our appendix for more details.

4.3 Ablation Studies

Settings: We employ GuideNet [64] as the default backbone. The model is pre-trained for 300 epochs and fine-tuned for 100 epochs on every dataset. The mask is randomly generated following [76,25] with different sizes and ratios.

(1) Masking strategy.

(i) We explore how to corrupt RGB-D data during pre-training in Table 2. We can find that shielding only RGB, only Depth, or RGB-D without shared

⁴ <https://vcl3d.github.io/Pano3D/download/>

⁵ <http://buildingparser.stanford.edu/dataset.html>

⁶ <https://vcl3d.github.io/3D60/>

Masked Data	Shared Mask	Mask Ratio	Mask Size			
			4	8	16	32
RGB	-	0.75	195.7	198.1	194.0	196.2
D	-		190.7	177.6	186.1	203.3
RGB-D	No		183.4	178.5	182.2	193.0
RGB-D	Yes		166.8	168.9	167.6	169.9

Table 2. Ablation on different masked input data on Stanford2D3D dataset, where the metric is RMSE (mm). The error of baseline without pre-training is **196.7**.

Mask Size	4			8			16						32		
Mask Ratio	0.45	0.6	0.75	0.45	0.6	0.75	0.15	0.3	0.45	0.6	0.75	0.9	0.45	0.6	0.75
RMSE	172.4	170.3	168.8	171.2	169.3	168.9	173.5	169.4	168.9	169.7	167.6	169.3	173.7	172.4	169.9

Table 3. Ablation on different mask sizes and mask ratios on Stanford2D3D dataset.

mask, all of which lead to worse performances because these operations destroy the model’s learning of unknown areas. In contrast, the model achieves the best results when employing the proposed shared random mask, indicating that corrupting the same areas can contribute to improvement for multi-modal vision tasks. The following experiments are based on the random shared mask.

(ii) We study the effect of different mask sizes and ratios on the model’s representation learning in Table 3. First, the model performs better when the mask size is changed from 4 to 16. We hold the opinion that the larger mask urges the model to learn long-range dependency between invisible and visible pixels. However, when setting the mask size to 32, the model has a degraded performance as it is too large to establish remote dependency. Second, when the mask size is set to 16, the model tends to perform better from 15% to 90% ratios, which could enforce the model to predict more unseen areas and acquires representation that is closer to the real domain.

(2) Number of pre-training epochs and data amounts.

(i) The left of Figure 5 demonstrates the influence of different pre-training epochs on fine-tuning, and the right shows the loss of pre-training. We can find that the model’s error gradually decreases with the increase of pre-training epochs. This is because the model can learn better representation with more epochs, which is also reflected in the lower loss in the right of Figure 5. For the trade-off between speed and accuracy, unless otherwise stated, we pre-train the model for 300 epochs by default.

(ii) Table 4 explores the effect of different data amounts for pre-training on fine-tuning. For a fair comparison, we report the results of the 400th epoch without pre-training, whose cost roughly aligns with the setting of pre-training for 300 epochs and fine-tuning for 100 epochs. It can be found that without pre-training, the performance of 400 epochs has no improvements over 100 epochs. However, when conducting M³PT just on single dataset, it leads to 12.9% improvements averagely on three datasets, demonstrating the significant effectiveness of M³PT. Further, when pre-training on all the data of these three datasets, the performances are always superior to that only using a single dataset. Therefore, it is concluded that more data involved in M³PT can consistently prevents the overfitting risks during fine-tuning.

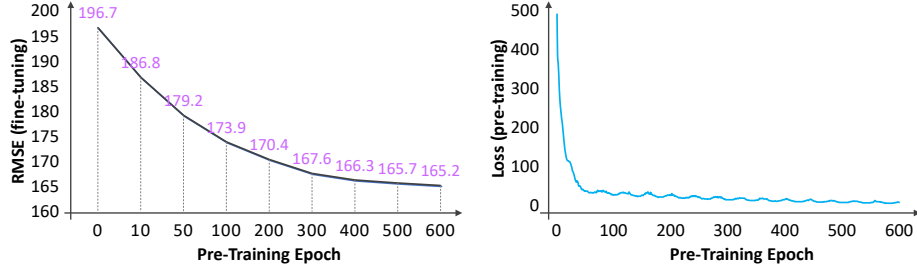


Fig. 5. Ablation on different pre-training epochs with mask size 16 and mask ratio 0.75 on Stanford2D3D dataset. The loss value is magnified by 10^4 for clear visualization.

Dataset	Data amount	w/o Pret. (100 epochs)	w/o Pret. (400 epochs)	Pret. on Self Data (300+100 epochs)	Pret. on All Data (300+100 epochs)
Matterport3D	5.6k	168.1	168.5	146.2	138.9
Stanford2D3D	1k	196.7	196.3	167.6	149.0
3D60	6.7k	159.9	160.2	142.3	127.2

Table 4. Ablation on different data amounts used during pre-training (Pret.). The mask size and ratio are 16 and 0.75, respectively. “300+100 epochs” denotes 300 pre-training epochs and 100 fine-tuning epochs.

4.4 Comparisons with SoTA Methods

In this subsection, we compare with recent SoTA works, including UniFuse [30], HoHoNet [63], PENet [27], and GuideNet [64]. HoHo-R and HoHo-H severally refer to using ResNet [26] and HardNet [9] as its backbone. Table 5 and Figure 6 demonstrate the quantitative and qualitative results, respectively. Based on different baselines, Figure 7 further shows the influence of additional sparse depth information and proposed M³PT on the recovery of panoramic depth.

(1) Quantitative results.

Overall, as illustrated in Table 5, the proposed M³PT is consistently superior to other methods in all metrics on three datasets.

(i) On Matterport3D dataset, M³PT greatly exceeds the second-best HoHo-R by 53.8%, 51.7%, and 37.9% in MRE, MAE, and RMSElog, severally. Compared with the suboptimal GuideNet in RMSE, the error is reduced from 192.9mm to 138.9mm, improving the performance nearly by 28.0%. Besides, M³PT achieves the highest accuracies in δ_i with different thresholds, outperforming the second-best method by 1.21, 0.29, and 0.09 percent point in δ_1 , δ_2 , and δ_3 , respectively.

(ii) On Stanford2D3D dataset, M³PT is superior to the suboptimal UniFuse with 44.0% improvement in MRE. Also, the MAE, RMSE, RMSElog is severally reduced by 42.6%, 24.3%, and 30.8% when comparing M³PT with the second-best GuideNet. In addition, the accuracy metric verifies the effectiveness of M³PT again, which plays a prominent role in all approaches.

(iii) On 3D60 dataset, M³PT surpasses the second-best HoHo-R with large margins, improving it by 57.4% in MRE, 54.9% in MAE, 35.4% in RMSE, and 43.9% in RMSElog, severally. Furthermore, M³PT is more accurate than other

Dataset	Method	Error Metric ↓				Accuracy Metric ↑		
		MRE	MAE	RMSE	RMSElog	$\delta_{1.25}$	$\delta_{1.25^2}$	$\delta_{1.25^3}$
Matterport3D	UniFuse [30]	0.0475	95.2	229.1	0.0381	0.9710	0.9924	0.9970
	HoHo-R [63]	<u>0.0355</u>	<u>75.0</u>	199.2	<u>0.0311</u>	<u>0.9806</u>	0.9945	0.9977
	HoHo-H [63]	0.0406	85.7	215.5	0.0337	0.9772	0.9938	0.9975
	ENet [27]	0.1317	242.4	319.6	0.0730	0.9141	0.9922	0.9969
	PENet [27]	0.0493	91.5	248.0	0.0350	0.9728	0.9935	0.9970
	GuideNet [64]	0.0438	87.2	<u>192.9</u>	0.0327	<u>0.9806</u>	<u>0.9948</u>	<u>0.9981</u>
	Our M³PT	0.0164	36.2	138.9	0.0193	0.9927	0.9976	0.9990
Stanford2D3D	UniFuse [30]	<u>0.0489</u>	93.4	216.2	0.0392	0.9661	0.9919	0.9973
	HoHo-R [63]	0.0677	123.9	242.5	0.0478	0.9463	0.9862	0.9959
	HoHo-H [63]	0.0695	127.9	254.8	0.0497	0.9434	0.9852	0.9957
	ENet [27]	0.1645	299.3	415.3	0.1590	0.8471	0.9130	0.9878
	PENet [27]	0.0530	95.9	200.6	0.0404	<u>0.9694</u>	<u>0.9934</u>	<u>0.9981</u>
	GuideNet [27]	0.0506	<u>92.1</u>	<u>196.7</u>	<u>0.0380</u>	0.9689	0.9926	0.9978
	Our M³PT	0.0274	52.9	149.0	0.0263	0.9859	0.9963	0.9988
3D60	UniFuse [30]	0.0446	94.1	215.6	0.0342	0.9749	0.9947	0.9984
	HoHo-R [63]	<u>0.0338</u>	<u>75.6</u>	<u>196.9</u>	<u>0.0294</u>	<u>0.9818</u>	0.9954	0.9983
	HoHo-H [63]	0.0376	81.9	205.8	0.0317	0.9788	0.9947	0.9981
	ENet [27]	0.0961	190.2	272.9	0.0558	0.9706	<u>0.9956</u>	0.9983
	PENet [27]	0.0680	120.3	233.9	0.0321	0.9743	0.9926	0.9980
	GuideNet [27]	0.0689	144.2	239.3	0.0418	0.9711	0.9954	<u>0.9987</u>
	Our M³PT	0.0144	34.1	127.2	0.0165	0.9944	0.9985	0.9995

Table 5. Quantitative comparisons of panoramic depth completion on three datasets. The best and the second best results are highlighted in bold and underline, respectively.

approaches and prevail over the suboptimal methods with 1.26, 0.29, and 0.08 percent point in δ_1 , δ_2 , and δ_3 , respectively.

(iv) Last but not least, apart from GuideNet that has been reported in Table 5, we further employ UniFuse, HoHo-R, and HoHo-H as baselines to see the influence of the additional sparse depth data and proposed mask strategy on the recovery of panoramic depth. As shown in Figure 7, gray bar: only using RGB, orange bar: using both RGB and its sparse depth, and blue bar: using RGB and sparse depth with the proposed mask strategy M³PT. We can find that adding sparse depth data can benefit models with very large margins. Specifically, the errors of UniFuse, HoHo-R, and HoHo-H are severally reduced by 55.8%, 41.5%, and 50.5% on average on three datasets. What’s more, adopting M³PT contributes to their significant improvements of 27.0%, 25.4%, and 26.3% on average compared with the orange bars on three datasets. These facts indicate sparse depth information has great reference value for depth recovery, and also prove that the panoramic depth completion is a potentially valuable task.

In short, all above numerical results demonstrate the effectiveness of M³PT.

(2) Qualitative results.

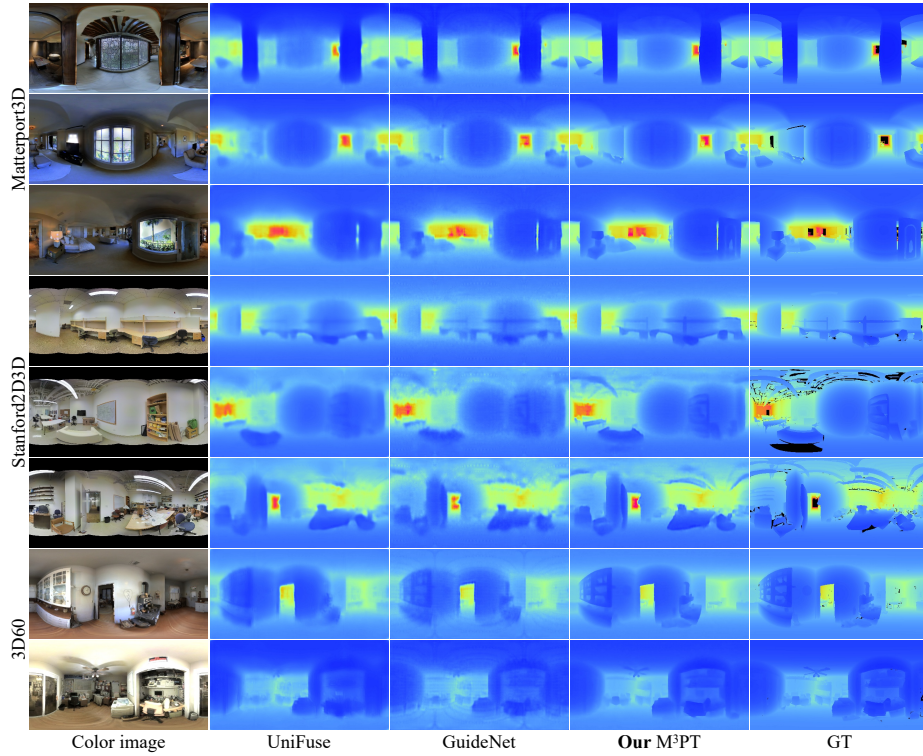


Fig. 6. Qualitative comparison of different methods, including UniFuse [30], GuideNet [64], and our M³PT. More visualizations can be found in our supplementary material.

(i) As shown in Figure 6, our M³PT can recover more detailed objects and precise depth with reasonable visual effect. For example, for one thing, as illustrated in the first, fourth, and seventh rows, M³PT succeeds in predicting clearer edges of doors, tables, chairs, windows, etc. For another thing, as shown in the fifth and sixth rows, although the color images of Stanford2D3D do not have pixels at both the top and bottom, M³PT can still predict more accurate depth values in the invisible areas. It strongly demonstrates the effectiveness and generalization of the proposed masked pre-training strategy via corrupting RGB-D data. In addition, M³PT is also good at distinguishing from background and foreground, *e.g.*, the furniture can be clearly discriminated from the wall.

(ii) As illustrated in Figure 8, based on only color images (PDE), the depth predicted by UniFuse is extremely blurry that the corresponding 3D reconstruction introduces plenty of wrong location information, which causes negative deformation, especially nearby walls. By contrast, adding sparse depth data (PDC) vastly improves the visual effect of both depth recovery and 3D reconstruction. Furthermore, when deploying the proposed M³PT with RGB-D data as input, both objects' structures and details tend to be more clear and abundant.

In summary, all these visual clues verify that M³PT has robust capability of recovering panoramic depth from 360° monocular RGB-D data.

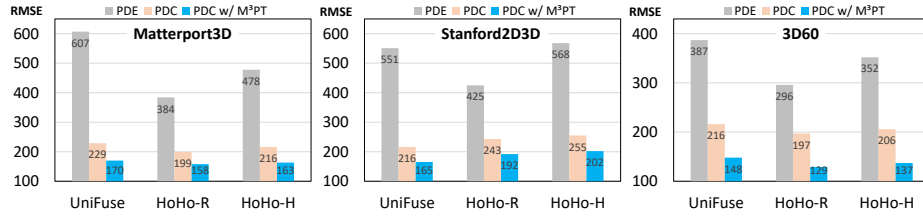


Fig. 7. Comparisons of different baselines with different-modal input data and M³PT. PDE: panoramic depth estimation only from color images. PDC: panoramic depth completion from not only color images but the corresponding sparse depths.

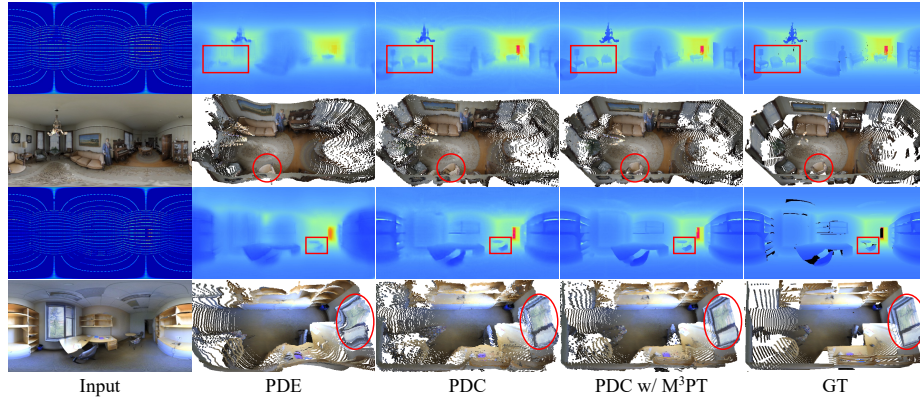


Fig. 8. Visual results of UniFuse [30] with different-modal input data and M³PT.

5 Conclusion

In this paper, we introduced a potentially valuable task, *i.e.*, panoramic depth completion, to help with dense panoramic depth recovery and 3D reconstruction from monocular 360° RGB-D data. Furthermore, we proposed the multi-modal masked pre-training (M³PT) framework to handle this task. It was the first time we showed that the masked pre-training could be very effective in modeling multi-modal tasks for vision, instead of the single-modal image recognition which was popularized by the masked autoencoders (MAE). As a result, comprehensive evaluations demonstrated the superiority of M³PT on three benchmark datasets. At last, we hope our exploration in this paper can facilitate future studies concerned with multi-modal vision tasks. In the future, we are going to extend M³PT to related topics such as depth denoising and super-resolution.

6 Acknowledgement

The authors would like to thank reviewers for their detailed comments and instructive suggestions. This work was supported by the National Science Fund of China under Grant No. U1713208, 62072242 and Postdoctoral Innovative Talent Support Program of China under Grant BX20200168, 2020M681608.

References

1. Aich, S., Vianney, J.M.U., Islam, M.A., Liu, M.K.B.: Bidirectional attention network for monocular depth estimation. In: ICRA. pp. 11746–11752. IEEE (2021) [4](#)
2. Albanis, G., Zioulis, N., Drakoulis, P., Gkitsas, V., Sterzentsenko, V., Alvarez, F., Zarpalas, D., Daras, P.: Pano3d: A holistic benchmark and a solid baseline for 360° depth estimation. In: CVPRW. pp. 3722–3732. IEEE (2021) [2](#), [3](#), [9](#)
3. Armeni, I., Sax, S., Zamir, A.R., Savarese, S.: Joint 2d-3d-semantic data for indoor scene understanding. arXiv preprint arXiv:1702.01105 (2017) [3](#), [5](#), [9](#)
4. Bai, J., Lai, S., Qin, H., Guo, J., Guo, Y.: Glpanodepth: Global-to-local panoramic depth estimation. arXiv preprint arXiv:2202.02796 (2022) [2](#), [6](#)
5. Bao, H., Dong, L., Wei, F.: Beit: Bert pre-training of image transformers. arXiv preprint arXiv:2106.08254 (2021) [6](#)
6. Bian, J., Li, Z., Wang, N., Zhan, H., Shen, C., Cheng, M.M., Reid, I.: Unsupervised scale-consistent depth and ego-motion learning from monocular video. In: NeurIPS (2019) [4](#)
7. Casser, V., Pirk, S., Mahjourian, R., Angelova, A.: Depth prediction without the sensors: Leveraging structure for unsupervised learning from monocular videos. In: AAAI. vol. 33, pp. 8001–8008 (2019) [4](#)
8. Chang, A., Dai, A., Funkhouser, T., Halber, M., Niessner, M., Savva, M., Song, S., Zeng, A., Zhang, Y.: Matterport3d: Learning from rgb-d data in indoor environments. In: 3DV (2017) [5](#)
9. Chao, P., Kao, C.Y., Ruan, Y.S., Huang, C.H., Lin, Y.L.: Hardnet: A low memory traffic network. In: ICCV. pp. 3552–3561 (2019) [11](#)
10. Chen, M., Radford, A., Child, R., Wu, J., Jun, H., Luan, D., Sutskever, I.: Generative pretraining from pixels. In: ICML. pp. 1691–1703. PMLR (2020) [6](#)
11. Cheng, X., Wang, P., Guan, C., Yang, R.: Cspn++: Learning context and resource aware convolutional spatial propagation networks for depth completion. In: AAAI. pp. 10615–10622 (2020) [5](#)
12. Cheng, X., Wang, P., Yang, R.: Learning depth with convolutional spatial propagation network. In: ECCV. pp. 103–119 (2018) [5](#)
13. Chodosh, N., Wang, C., Lucey, S.: Deep convolutional compressed sensing for lidar depth completion. In: ACCV. pp. 499–513. Springer (2018) [5](#)
14. Dosovitskiy, A., Beyer, L., Kolesnikov, A., Weissenborn, D., Zhai, X., Unterthiner, T., Dehghani, M., Minderer, M., Heigold, G., Gelly, S., et al.: An image is worth 16x16 words: Transformers for image recognition at scale. In: ICLR (2021) [6](#)
15. Eder, M., Moulon, P., Guan, L.: Pano popups: Indoor 3d reconstruction with a plane-aware network. In: 3DV. pp. 76–84. IEEE (2019) [5](#)
16. Eigen, D., Puhrsch, C., Fergus, R.: Depth map prediction from a single image using a multi-scale deep network. In: NeurIPS. pp. 2366–2374 (2014) [4](#)
17. Eldesokey, A., Felsberg, M., Khan, F.S.: Confidence propagation through cnns for guided sparse depth regression. IEEE transactions on pattern analysis and machine intelligence **42**(10), 2423–2436 (2019) [5](#)
18. Erhan, D., Bengio, Y., Courville, A., Manzagol, P.A., Vincent, P., Bengio, S.: Why does unsupervised pre-training help deep learning? Journal of Machine Learning Research **11**, 625–660 (2010) [2](#), [3](#)
19. Feng, B.Y., Yao, W., Liu, Z., Varshney, A.: Deep depth estimation on 360 images with a double quaternion loss. In: 3DV. pp. 524–533. IEEE (2020) [6](#)

20. Feng, Q., Shum, H.P., Morishima, S.: 360 depth estimation in the wild—the depth360 dataset and the segfuse network. In: VR. IEEE (2022) [6](#)
21. Godard, C., Mac Aodha, O., Firman, M., Brostow, G.J.: Digging into self-supervised monocular depth estimation. In: ICCV. pp. 3828–3838 (2019) [4](#)
22. Gordon, A., Li, H., Jonschkowski, R., Angelova, A.: Depth from videos in the wild: Unsupervised monocular depth learning from unknown cameras. In: ICCV. pp. 8977–8986 (2019) [2](#), [4](#)
23. Gu, J., Xiang, Z., Ye, Y., Wang, L.: Denselidar: A real-time pseudo dense depth guided depth completion network. IEEE Robotics and Automation Letters **6**(2), 1808–1815 (2021) [5](#)
24. Guizilini, V., Ambrus, R., Pillai, S., Raventos, A., Gaidon, A.: 3d packing for self-supervised monocular depth estimation. In: CVPR. pp. 2485–2494 (2020) [4](#)
25. He, K., Chen, X., Xie, S., Li, Y., Dollár, P., Girshick, R.: Masked autoencoders are scalable vision learners. arXiv preprint arXiv:2111.06377 (2021) [3](#), [6](#), [8](#), [9](#)
26. He, K., Zhang, X., Ren, S., Sun, J.: Deep residual learning for image recognition. In: CVPR. pp. 770–778 (2016) [11](#)
27. Hu, M., Wang, S., Li, B., Ning, S., Fan, L., Gong, X.: Penet: Towards precise and efficient image guided depth completion. In: ICRA (2021) [5](#), [11](#), [12](#)
28. Ioffe, S., Szegedy, C.: Batch normalization: Accelerating deep network training by reducing internal covariate shift. In: ICML. pp. 448–456. PMLR (2015) [20](#)
29. Jaritz, M., De Charette, R., Wirbel, E., Perrotton, X., Nashashibi, F.: Sparse and dense data with cnns: Depth completion and semantic segmentation. In: 3DV. pp. 52–60 (2018) [5](#)
30. Jiang, H., Sheng, Z., Zhu, S., Dong, Z., Huang, R.: Unifuse: Unidirectional fusion for 360 panorama depth estimation. IEEE Robotics and Automation Letters **6**(2), 1519–1526 (2021) [2](#), [6](#), [8](#), [11](#), [12](#), [13](#), [14](#), [26](#)
31. Jin, L., Xu, Y., Zheng, J., Zhang, J., Tang, R., Xu, S., Yu, J., Gao, S.: Geometric structure based and regularized depth estimation from 360 indoor imagery. In: CVPR. pp. 889–898 (2020) [6](#)
32. Klingner, M., Termöhlen, J.A., Mikolajczyk, J., Fingscheidt, T.: Self-supervised monocular depth estimation: Solving the dynamic object problem by semantic guidance. In: ECCV. pp. 582–600 (2020) [4](#)
33. Krauss, B., Schroeder, G., Gustke, M., Hussein, A.: Deterministic guided lidar depth map completion. arXiv preprint arXiv:2106.07256 (2021) [5](#)
34. Lai, Z., Chen, D., Su, K.: Olanet: Self-supervised 360° depth estimation with effective distortion-aware view synthesis and l1 smooth regularization. In: ICME. pp. 1–6. IEEE (2021) [6](#)
35. Lee, J.H., Han, M.K., Ko, D.W., Suh, I.H.: From big to small: Multi-scale local planar guidance for monocular depth estimation. In: CVPR (2020) [4](#)
36. Lee, S., Lee, J., Kim, B., Yi, E., Kim, J.: Patch-wise attention network for monocular depth estimation. In: AAAI. vol. 35, pp. 1873–1881 (2021) [4](#)
37. Lee, Y., Jeong, J., Yun, J., Cho, W., Yoon, K.J.: Spherephd: Applying cnns on a spherical polyhedron representation of 360deg images. In: CVPR. pp. 9181–9189 (2019) [5](#)
38. Lee, Y., Jeong, J., Yun, J., Cho, W., Yoon, K.J.: Spherephd: Applying cnns on 360° images with non-euclidean spherical polyhedron representation. IEEE Transactions on Pattern Analysis and Machine Intelligence (2020) [5](#)
39. Li, A., Yuan, Z., Ling, Y., Chi, W., Zhang, C., et al.: A multi-scale guided cascade hourglass network for depth completion. In: WACV. pp. 32–40 (2020) [5](#)

40. Li, J., Zhang, T., Luo, W., Yang, J., Yuan, X.T., Zhang, J.: Sparseness analysis in the pretraining of deep neural networks. *IEEE transactions on neural networks and learning systems* **28**(6), 1425–1438 (2016) [2](#)
41. Li, Y., Yan, Z., Duan, Y., Ren, L.: Panodepth: A two-stage approach for monocular omnidirectional depth estimation. In: *3DV*. pp. 648–658. IEEE (2021) [2](#), [6](#)
42. Lin, Y., Cheng, T., Zhong, Q., Zhou, W., Yang, H.: Dynamic spatial propagation network for depth completion. In: *AAAI* (2022) [5](#)
43. Liu, L., Song, X., Lyu, X., Diao, J., Wang, M., Liu, Y., Zhang, L.: Fcfr-net: Feature fusion based coarse-to-fine residual learning for depth completion. In: *AAAI*. vol. 35, pp. 2136–2144 (2021) [5](#)
44. Liu, L., Song, X., Wang, M., Liu, Y., Zhang, L.: Self-supervised monocular depth estimation for all day images using domain separation. In: *ICCV*. pp. 12737–12746 (2021) [4](#)
45. Loshchilov, I., Hutter, F.: Sgdr: Stochastic gradient descent with warm restarts. In: *ICLR* (2017) [20](#)
46. Loshchilov, I., Hutter, F.: Decoupled weight decay regularization. In: *ICLR* (2019) [20](#)
47. Lu, K., Barnes, N., Anwar, S., Zheng, L.: From depth what can you see? depth completion via auxiliary image reconstruction. In: *CVPR*. pp. 11306–11315 (2020) [5](#)
48. Ma, F., Cavalheiro, G.V., Karaman, S.: Self-supervised sparse-to-dense: Self-supervised depth completion from lidar and monocular camera. In: *ICRA* (2019) [5](#)
49. Meng, Y., Lu, Y., Raj, A., Sunarjo, S., Guo, R., Javidi, T., Bansal, G., Bharamdia, D.: Signet: Semantic instance aided unsupervised 3d geometry perception. In: *CVPR*. pp. 9810–9820 (2019) [4](#)
50. Park, J., Joo, K., Hu, Z., Liu, C.K., Kweon, I.S.: Non-local spatial propagation network for depth completion. In: *ECCV* (2020) [5](#)
51. Pintore, G., Agus, M., Almansa, E., Schneider, J., Gobbetti, E.: Slicenet: deep dense depth estimation from a single indoor panorama using a slice-based representation. In: *CVPR*. pp. 11536–11545 (2021) [2](#), [6](#), [9](#)
52. Qiao, S., Zhu, Y., Adam, H., Yuille, A., Chen, L.C.: Vip-deeplab: Learning visual perception with depth-aware video panoptic segmentation. In: *CVPR*. pp. 3997–4008 (2021) [4](#)
53. Qiu, J., Cui, Z., Zhang, Y., Zhang, X., Liu, S., Zeng, B., Pollefeys, M.: Deeplidar: Deep surface normal guided depth prediction for outdoor scene from sparse lidar data and single color image. In: *CVPR*. pp. 3313–3322 (2019) [5](#)
54. Ranjan, A., Jampani, V., Balles, L., Kim, K., Sun, D., Wulff, J., Black, M.J.: Competitive collaboration: Joint unsupervised learning of depth, camera motion, optical flow and motion segmentation. In: *CVPR*. pp. 12240–12249 (2019) [4](#)
55. Rey-Area, M., Yuan, M., Richardt, C.: 360monodepth: High-resolution 360° monocular depth estimation. *arXiv e-prints* pp. arXiv–2111 (2021) [6](#)
56. Roy, A., Todorovic, S.: Monocular depth estimation using neural regression forest. In: *CVPR*. pp. 5506–5514 (2016) [4](#)
57. Saxena, A., Chung, S.H., Ng, A.Y., et al.: Learning depth from single monocular images. In: *NeurIPS*. pp. 1–8 (2005) [4](#)
58. Schuster, R., Wasenmuller, O., Unger, C., Stricker, D.: Ssgp: Sparse spatial guided propagation for robust and generic interpolation. In: *WACV*. pp. 197–206 (2021) [5](#)
59. Shu, C., Yu, K., Duan, Z., Yang, K.: Feature-metric loss for self-supervised learning of depth and egomotion. In: *ECCV* (2020) [4](#)

60. Silberman, N., Hoiem, D., Kohli, P., Fergus, R.: Indoor segmentation and support inference from rgb-d images. In: ECCV. pp. 746–760. Springer (2012) [5](#)
61. Song, S., Yu, F., Zeng, A., Chang, A.X., Savva, M., Funkhouser, T.: Semantic scene completion from a single depth image. In: CVPR. pp. 1746–1754 (2017) [9](#)
62. Sun, C., Hsiao, C.W., Wang, N.H., Sun, M., Chen, H.T.: Indoor panorama planar 3d reconstruction via divide and conquer. In: CVPR. pp. 11338–11347 (2021) [6](#)
63. Sun, C., Sun, M., Chen, H.T.: Hohonet: 360 indoor holistic understanding with latent horizontal features. In: CVPR. pp. 2573–2582 (2021) [2](#), [6](#), [8](#), [9](#), [11](#), [12](#)
64. Tang, J., Tian, F.P., Feng, W., Li, J., Tan, P.: Learning guided convolutional network for depth completion. IEEE Transactions on Image Processing **30**, 1116–1129 (2020) [5](#), [8](#), [9](#), [11](#), [12](#), [13](#), [20](#), [26](#)
65. Tateno, K., Navab, N., Tombari, F.: Distortion-aware convolutional filters for dense prediction in panoramic images. In: ECCV. pp. 707–722 (2018) [5](#)
66. Teutscher, D., Mangat, P., Wasenmüller, O.: Pdc: Piecewise depth completion utilizing superpixels. In: ITSC. pp. 2752–2758. IEEE (2021) [5](#)
67. Uhrig, J., Schneider, N., Schneider, L., Franke, U., Brox, T., Geiger, A.: Sparsity invariant cnns. In: 3DV. pp. 11–20 (2017) [5](#), [7](#)
68. Van Gansbeke, W., Neven, D., De Brabandere, B., Van Gool, L.: Sparse and noisy lidar completion with rgb guidance and uncertainty. In: MVA. pp. 1–6 (2019) [5](#)
69. Vaswani, A., Shazeer, N., Parmar, N., Uszkoreit, J., Jones, L., Gomez, A.N., Kaiser, L., Polosukhin, I.: Attention is all you need. In: NeurlPS. vol. 30 (2017) [6](#)
70. Wang, F.E., Yeh, Y.H., Sun, M., Chiu, W.C., Tsai, Y.H.: Bifuse: Monocular 360 depth estimation via bi-projection fusion. In: CVPR. pp. 462–471 (2020) [6](#)
71. Wang, K., Zhang, Z., Yan, Z., Li, X., Xu, B., Li, J., Yang, J.: Regularizing nighttime weirdness: Efficient self-supervised monocular depth estimation in the dark. In: ICCV. pp. 16055–16064 (2021) [4](#)
72. Wong, A., Cicek, S., Soatto, S.: Learning topology from synthetic data for unsupervised depth completion. IEEE Robotics and Automation Letters **6**(2), 1495–1502 (2021) [5](#)
73. Wong, A., Fei, X., Hong, B.W., Soatto, S.: An adaptive framework for learning unsupervised depth completion. IEEE Robotics and Automation Letters **6**(2), 3120–3127 (2021) [5](#)
74. Wong, A., Fei, X., Tsuei, S., Soatto, S.: Unsupervised depth completion from visual inertial odometry. IEEE Robotics and Automation Letters **5**(2), 1899–1906 (2020) [5](#)
75. Wong, A., Soatto, S.: Unsupervised depth completion with calibrated backprojection layers. In: ICCV (2021) [5](#)
76. Xie, Z., Zhang, Z., Cao, Y., Lin, Y., Bao, J., Yao, Z., Dai, Q., Hu, H.: Simmim: A simple framework for masked image modeling. arXiv preprint arXiv:2111.09886 (2021) [3](#), [6](#), [8](#), [9](#)
77. Xu, Y., Zhu, X., Shi, J., Zhang, G., Bao, H., Li, H.: Depth completion from sparse lidar data with depth-normal constraints. In: ICCV. pp. 2811–2820 (2019) [5](#)
78. Xu, Z., Yin, H., Yao, J.: Deformable spatial propagation networks for depth completion. In: ICIP. pp. 913–917. IEEE (2020) [5](#)
79. Yan, L., Liu, K., Gao, L.: Dan-conv: Depth aware non-local convolution for lidar depth completion. Electronics Letters **57**(20), 754–757 (2021) [5](#)
80. Yan, Z., Wang, K., Li, X., Zhang, Z., Xu, B., Li, J., Yang, J.: Rignet: Repetitive image guided network for depth completion. arXiv preprint arXiv:2107.13802 (2021) [5](#)
81. Yin, W., Liu, Y., Shen, C., Yan, Y.: Enforcing geometric constraints of virtual normal for depth prediction. In: ICCV. pp. 5684–5693 (2019) [4](#)

82. Yun, I., Lee, H.J., Rhee, C.E.: Improving 360 monocular depth estimation via non-local dense prediction transformer and joint supervised and self-supervised learning. In: arXiv preprint arXiv:2109.10563 (2021) [2](#), [6](#), [9](#)
83. Zhang, Z., Cui, Z., Xu, C., Jie, Z., Li, X., Yang, J.: Joint task-recursive learning for semantic segmentation and depth estimation. In: ECCV. pp. 235–251 (2018) [4](#)
84. Zhang, Z., Cui, Z., Xu, C., Jie, Z., Li, X., Yang, J.: Joint task-recursive learning for rgb-d scene understanding. IEEE transactions on pattern analysis and machine intelligence **42**(10), 2608–2623 (2019) [4](#)
85. Zhang, Z., Cui, Z., Xu, C., Yan, Y., Sebe, N., Yang, J.: Pattern-affinitive propagation across depth, surface normal and semantic segmentation. In: CVPR. pp. 4106–4115 (2019) [4](#)
86. Zhao, S., Gong, M., Fu, H., Tao, D.: Adaptive context-aware multi-modal network for depth completion. IEEE Transactions on Image Processing (2021) [5](#)
87. Zhao, W., Liu, S., Shu, Y., Liu, Y.J.: Towards better generalization: Joint depth-pose learning without posenet. In: CVPR. pp. 9151–9161 (2020) [4](#)
88. Zhou, K., Yang, K., Wang, K.: Panoramic depth estimation via supervised and unsupervised learning in indoor scenes. Applied Optics **60**(26), 8188–8197 (2021) [6](#)
89. Zhou, L., Cui, Z., Xu, C., Zhang, Z., Wang, C., Zhang, T., Yang, J.: Pattern-structure diffusion for multi-task learning. In: CVPR. pp. 4514–4523 (2020) [4](#)
90. Zhou, T., Brown, M., Snavely, N., Lowe, D.G.: Unsupervised learning of depth and ego-motion from video. In: CVPR. pp. 1851–1858 (2017) [4](#)
91. Zhu, Y., Dong, W., Li, L., Wu, J., Li, X., Shi, G.: Robust depth completion with uncertainty-driven loss functions. arXiv preprint arXiv:2112.07895 (2021) [5](#)
92. Zhuang, C., Lu, Z., Wang, Y., Xiao, J., Wang, Y.: Acdnet: Adaptively combined dilated convolution for monocular panorama depth estimation. In: AAAI (2022) [2](#), [6](#), [9](#)
93. Zioulis, N., Karakottas, A., Zarpalas, D., Alvarez, F., Daras, P.: Spherical view synthesis for self-supervised 360 depth estimation. In: 3DV. pp. 690–699. IEEE (2019) [3](#), [6](#), [9](#)
94. Zioulis, N., Karakottas, A., Zarpalas, D., Daras, P.: Omnidepth: Dense depth estimation for indoors spherical panoramas. In: ECCV. pp. 448–465 (2018) [5](#)
95. Zou, Y., Luo, Z., Huang, J.B.: Df-net: Unsupervised joint learning of depth and flow using cross-task consistency. In: ECCV. pp. 36–53 (2018) [4](#)

Supplementary Material for M³PT

Config	Value	
	pre-training	fine-tuning
optimizer	AdamW [46]	AdamW
learning rate schedule	CosineAnnealingLR [45]	MultiStepLR
learning rate	0.001	0.001
weight decay	0.01	0.01
optimizer momentum	$\beta_1, \beta_2 = 0.9, 0.999$	$\beta_1, \beta_2 = 0.9, 0.999$
batch size	92	92
augmentation	no	no

Table 6. Pre-training and fine-tuning settings.

A Overview

This document provides additional technical details and more visualization results. Specifically, in section B, we first describe the implementation details of M³PT. Next, we conduct additional experiments in section C. Finally, in section D, we show more visualizations of the depth prediction and 3D reconstruction on Matterport3D, Stanford2D3D, and 3D60 datasets.

B Implementation Details

Backbone architecture. We employ GuideNet [64] as the default architecture. It consists of two hourglass units, one for encoding RGB image input and another for modeling sparse depth input. Synchronized Cross-GPU Batch Normalization [28] is deployed. M³PT does *not* require any network structure adjustment when fine-tuning compared to pre-training.

Pre-training. The default setting is reported in Table 6. Our M³PT does *not* use additional data augmentation, including the color jittering and random horizontal flip conducted in GuideNet. We use cosine annealing learning rate strategy [45] with default ‘T_max=20, eta_min=0.00001, last_epoch=-1’.

Fine-tuning. The setting of fine-tuning is very similar with that of pre-training apart from the learning rate strategy with default ‘milestones=50, 100, 150, gamma=0.5, last_epoch=-1’, which is reported in Table 6.

C Additional Experiments

The metrics are mean relative error (MRE), mean absolute error (MAE), root mean square error of linear measures (RMSE), root mean square error of log measures (RMSElog), and δ_i referring to the percentage of predicted pixels whose

Dataset		pre-training & fine-tuning		
		Stanford2D3D	Matterport3D	3D60
testing	Stanford2D3D	167.7	159.4	248.5
	Matterport3D	254.7	146.2	224.3
	3D60	262.6	151.9	142.3

Table 7. Generalization capability of M³PT. We train it on one dataset but test on all three datasets. Best RMSE results of each column are marked in bold. The mask size and ratio on three datasets are 16 and 0.75, respectively.

relative error is within a threshold i that equals to 1.25 , 1.25^2 , and 1.25^3 . GT and P refer to ground-truth depth and predicted depth, respectively. Q_v denotes the set of valid pixels in GT . m is the number of valid pixels. Then the metrics are defined as

$$\begin{aligned}
- \text{MRE} &: \frac{1}{m} \sum_{q \in Q_v} \left| \frac{GT_q - P_q}{GT_q} \right| & - \text{RMSE} &: \sqrt{\frac{1}{m} \sum_{q \in Q_v} (GT_q - P_q)^2} \\
- \text{MAE} &: \frac{1}{m} \sum_{q \in Q_v} |GT_q - P_q| & - \delta_i &: \frac{1}{m} \left| \max \left(\frac{GT_q}{P_q}, \frac{P_q}{GT_q} \right) < 1.25^i \right| \\
- \text{RMSElog} &: \sqrt{\frac{1}{m} \sum_{q \in Q_v} (\log(GT_q) - \log(P_q))^2}
\end{aligned}$$

C.1 Testing on Different Datasets

Table 7 lists the generalization capability of M³PT. We pre-train and fine-tune M³PT on single dataset, but test it on all three datasets. In each column of Table 7, the performances of testing on other dataset is worse due to the different data distribution. We can also find that the generalization capability is weaker when training on Stanford2D3D, which is probably caused by the least amount of data and incomplete pixels of color images nearby the top and bottom areas. 3D60 dataset contains parts of Stanford2D3D and Matterport3D, which are potentially hard for models to generalize very well.

C.2 Reconstruction under Different Pre-Training Settings

Figure 10 demonstrates the reconstruction results of M³PT during pre-training on Stanford2D3D. As we can see that the model can partly recover depth clues given masked RGB-D pair and supervised by invisible areas of sparse depth, although the recovery is different from ground-truth depth annotation.

Figure 11 shows the generalization of M³PT which is pre-trained on Stanford2D3D but transferred to 3D60. Though the reconstruction results are far away from the ground-truth, it is probably plausible.

In addition, we also explore the generalization capability of M³PT under different mask settings. As shown in Figure 12, on Stanford2D3D, we test the model pre-trained with mask size 16 and ratio 0.75 on other mask sizes and ratios. We can find that the model can also recover depth clues in certain degree.

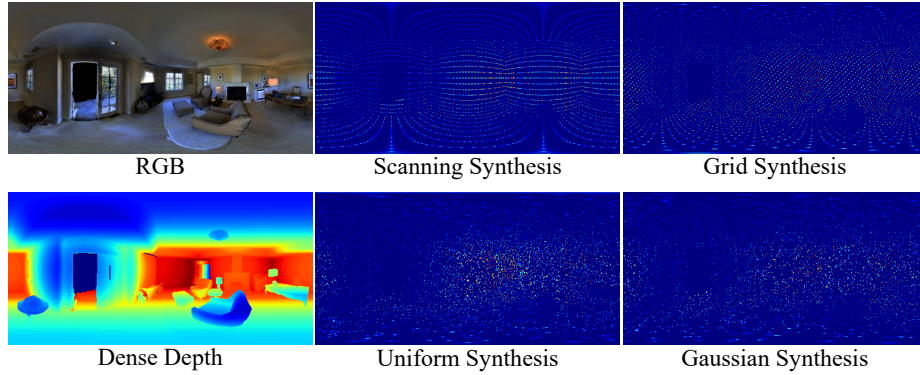


Fig. 9. Different patterns of data synthesis, including scanning, uniform, gaussian, and grid. Note that original cubical sampling results have been projected into equirectangular maps.

Pattern	Error Metric ↓				Accuracy Metric ↑		
	MRE	MAE	RMSE	RMSElog	$\delta_{1.25}$	$\delta_{1.25^2}$	$\delta_{1.25^3}$
Scanning	0.0274	52.9	149.0	0.0263	0.9859	0.9963	0.9988
Uniform	0.0598	121.3	227.7	0.0398	0.9764	0.9955	0.9984
Gaussian	0.0563	115.4	221.3	0.0384	0.9783	0.9957	0.9984
Grid	0.0511	104.6	195.8	0.0335	0.9851	0.9972	0.9991

Table 8. Generalization capability of M³PT on Stanford2D3D under different data synthesis patterns, which are shown in Figure 9.

C.3 Testing with Different Data Patterns

Table 8 reports the performances of M³PT with different data synthesis patterns. Note that the sparse depths of all patterns contain 6144 valid points, accounting for about 4.69% of the entire maps, shown in Figure 9. As we can see from Table 8, the scanning pattern can help to recover better depth, indicating it’s reasonable to synthesize sparse depths by imitating laser scanning.

D More Visualizations

This section shows more visualizations on three datasets. As illustrated in Figure 13, it is obviously that our M³PT can produce better depth predictions and 3D reconstructions than other related methods.

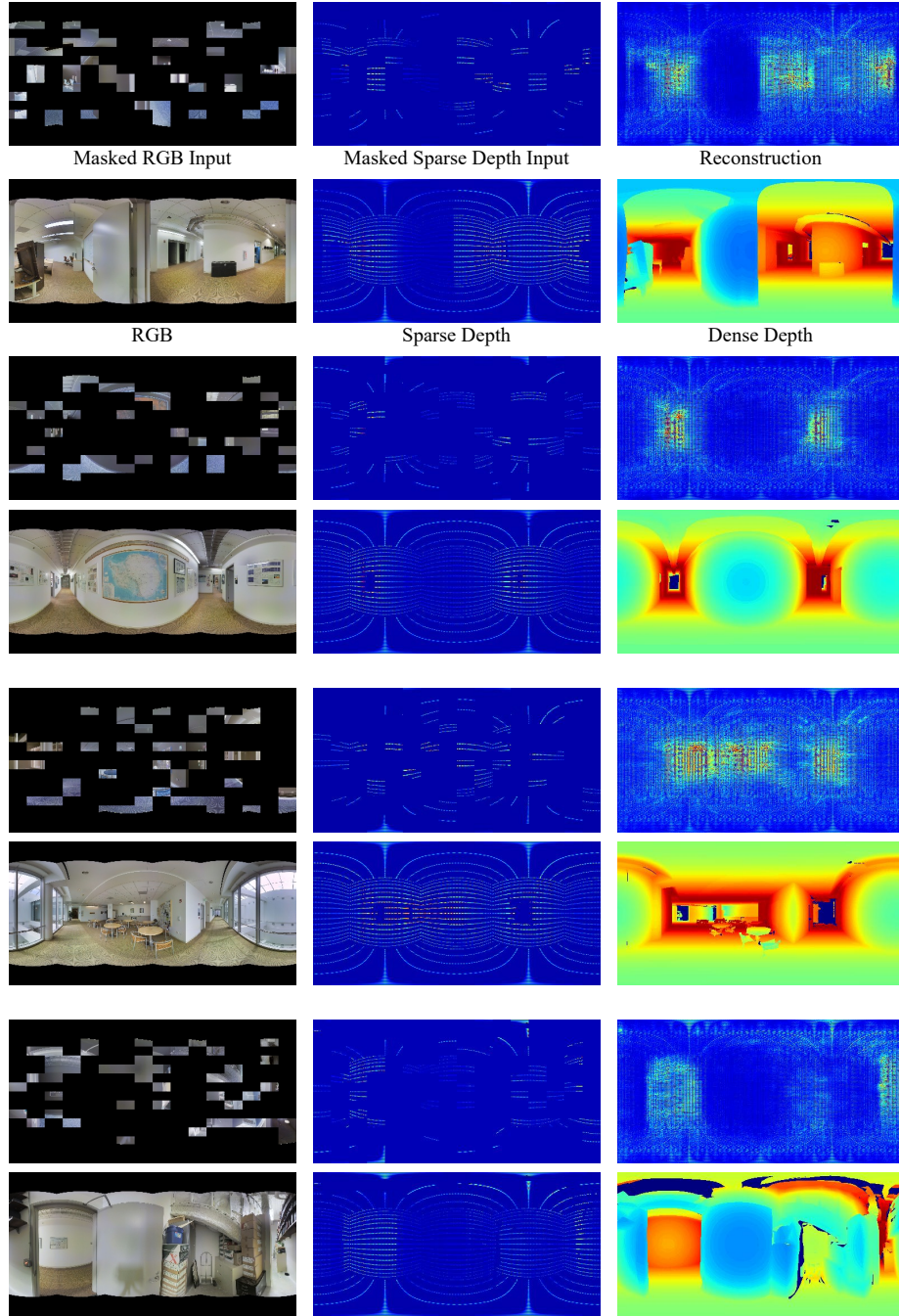


Fig. 10. Example of M³PT reconstructions during pre-training on **Stanford2D3D** testing split. The mask size is 16 and the mask ratio is 0.75. Best color of view.

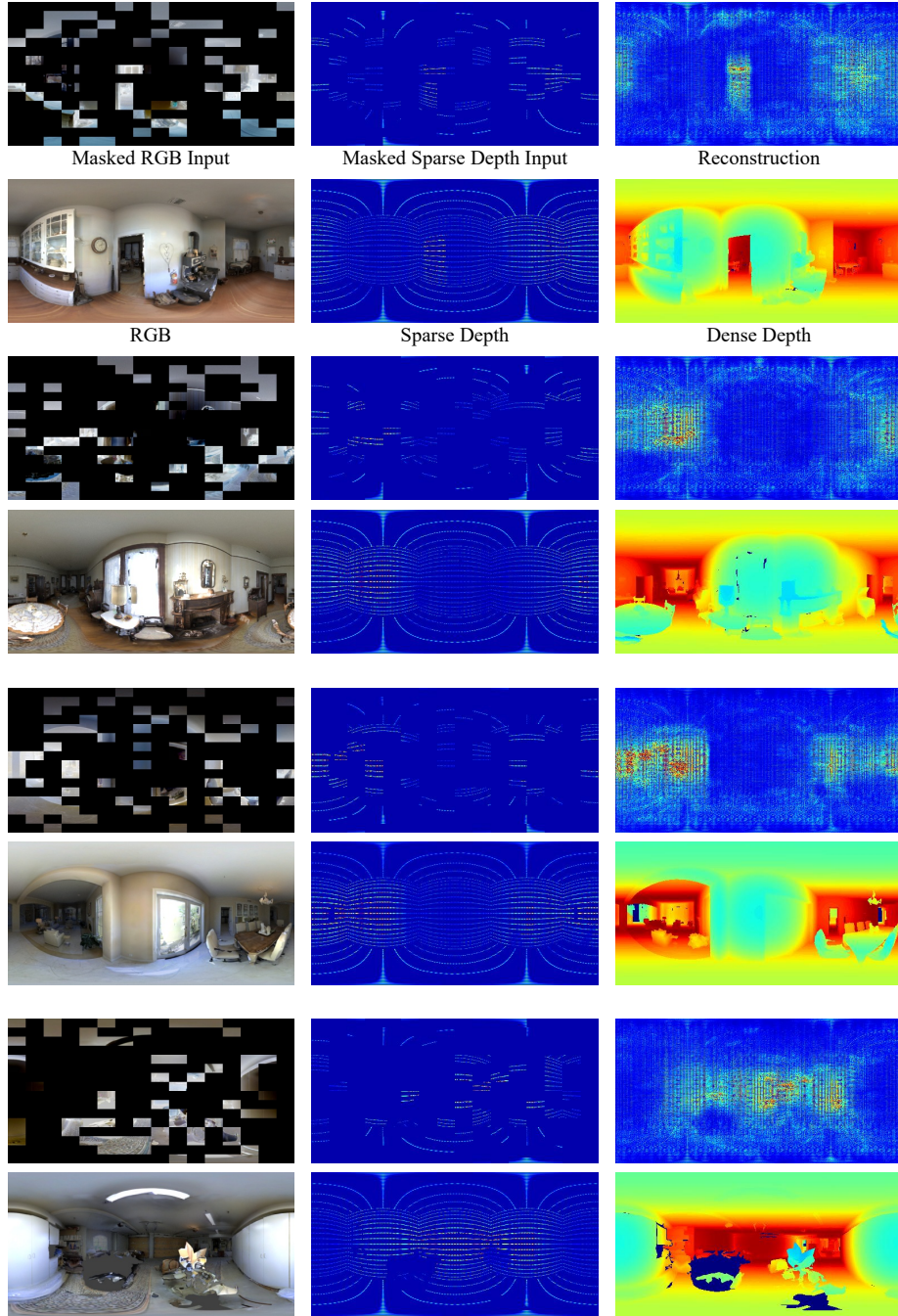


Fig. 11. Example of M³PT reconstructions during pre-training on 3D60 testing split, using M³PT pre-trained on Stanford2D3D (the same model weights as in Figure 10).

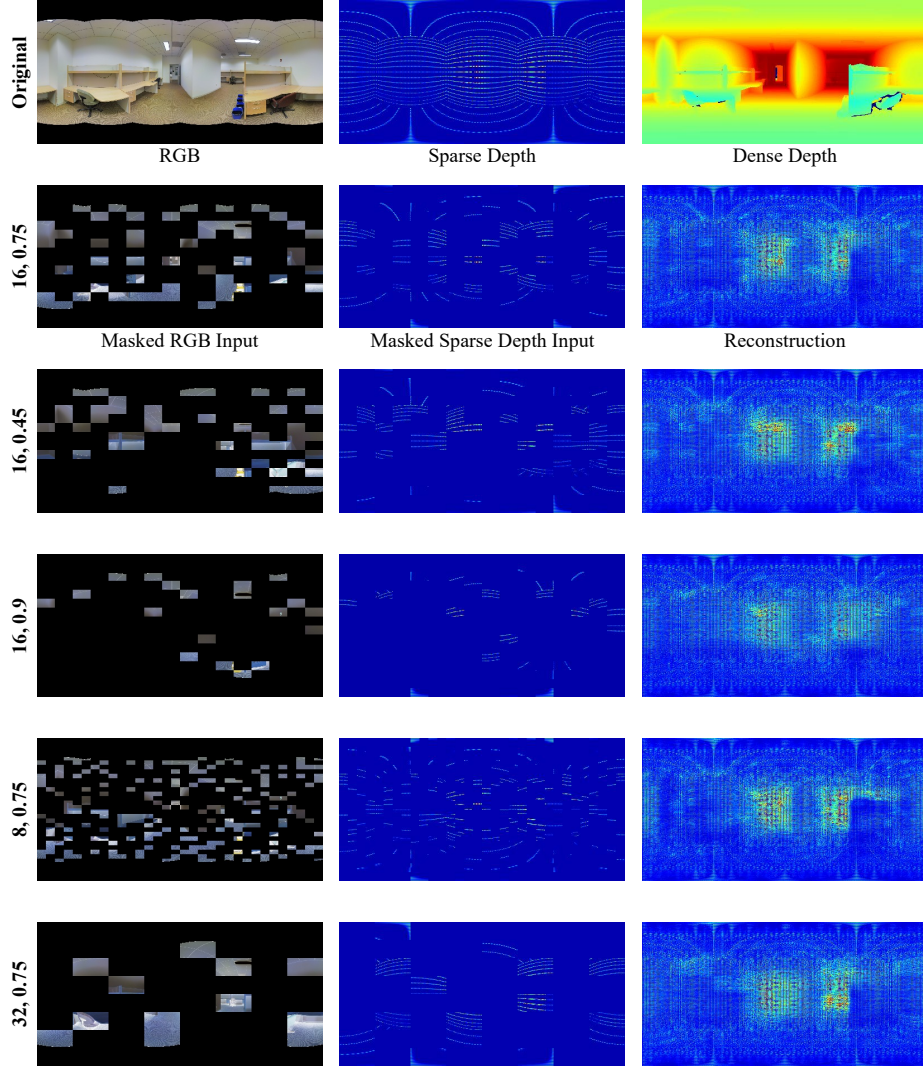


Fig. 12. Example of M³PT reconstructions during pre-training on Stanford2D3D testing split, using the M³PT with mask size 16 and mask ratio 0.75 that is pre-trained on Stanford2D3D (the same model weights as in Figure 10), but applied on inputs with different mask sizes and mask ratios.

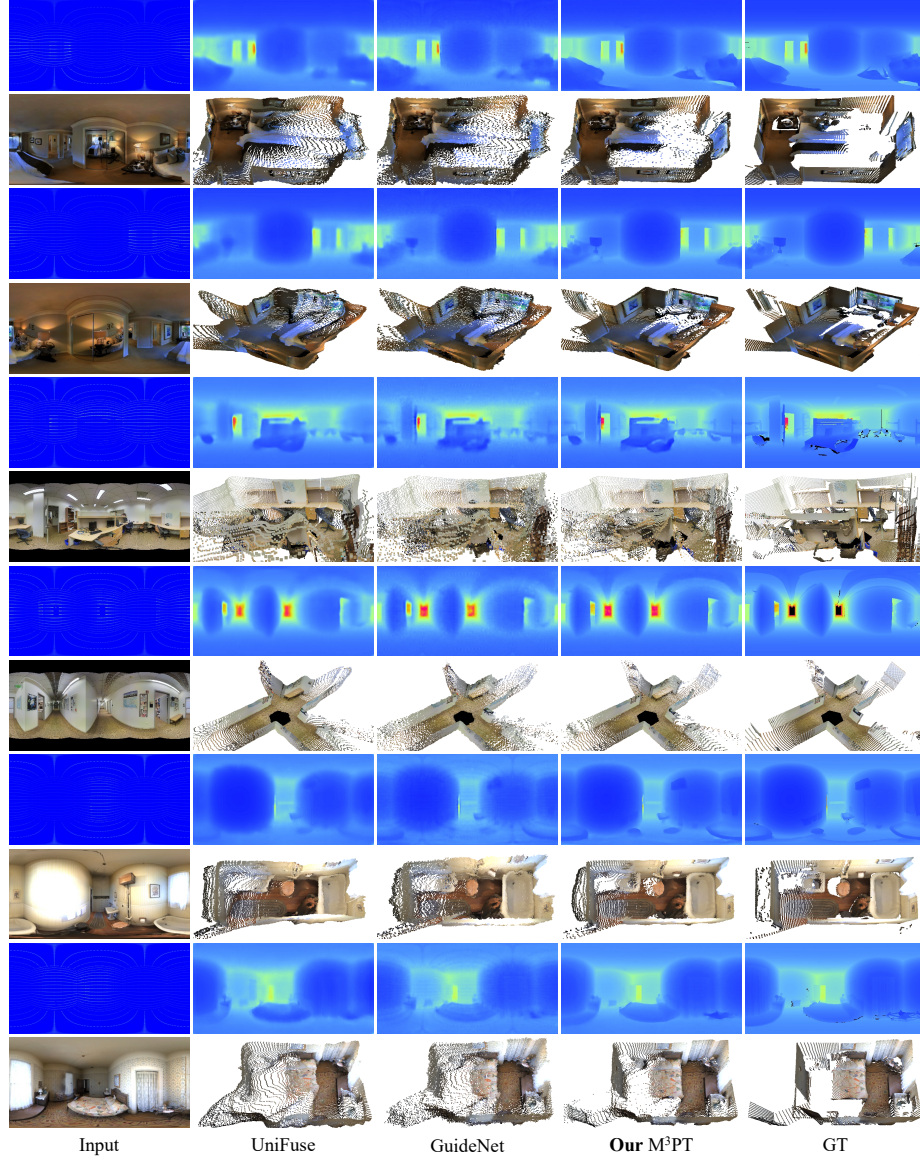


Fig. 13. Qualitative comparison of different methods, including UniFuse [30], GuideNet [64], and our M³PT on Matterport3D (the first four rows), Stanford2D3D (the second four rows), and 3D60 (the third four rows) datasets.